Nanoscale

PAPER

View Article Online
View Journal | View Issue

Check for updates

Cite this: *Nanoscale*, 2019, **11**, 3344

Polyethyleneimine-assisted one-pot synthesis of quasi-fractal plasmonic gold nanocomposites as a photothermal theranostic agent†

Vladimir Mulens-Arias, Alba Nicolás-Boluda, Alexandre Gehanno, Alice Balfourier, Florent Carn and Florence Gazeau *

Gold nanoparticles have been thoroughly used in designing thermal ablative therapies and in photoacoustic imaging in cancer treatment owing to their unique and tunable plasmonic properties. While the plasmonic properties highly depend on the size and structure, controllable aggregation of gold nanoparticles can trigger a plasmonic coupling of adjacent electronic clouds, henceforth leading to an increase of light absorption within the near-infrared (NIR) window. Polymer-engraftment of gold nanoparticles has been investigated to achieve the plasmonic coupling phenomenon, but complex chemical steps are often needed to accomplish a biomedically relevant product. An appealing and controllable manner of achieving polymer-based plasmon coupling is a template-assisted Au^{+3} reduction that ensures *in situ* gold reduction and coalescence. Among the polymers exploited as reducing agents are polyethyleneimines (PEI). In this study, we addressed the PEI-assisted synthesis of gold nanoparticles and their further aggregation to obtain fractal NIR-absorbent plasmonic nanoaggregates for photothermal therapy and photoacoustic imaging of colorectal cancer. PEI-assisted Au^{+3} reduction was followed up by UV-visible light absorption, small-angle X-ray scattering (SAXS), and photo-thermal conversion. The reaction kinetics, stability, and the photothermal plasmonic properties of the as-synthesized nanocomposites tightly depended on the PEI : Au ratio. We defined a PEI-Au ratio range (2.5–5) for the one-pot synthesis of gold nanoparticles that self-arrange into fractal nanoaggregates with demonstrated photo-thermal therapeutic and imaging efficiency both *in vitro* and *in vivo* in a colorectal carcinoma (CRC) animal model.

Received 5th December 2018,
Accepted 21st January 2019

DOI: 10.1039/c8nr09849b

rsc.li/nanoscale

Published on 21 janar 2019. Downloaded by Fail Open on 7.5.2025 9:29:04 e paradites.

1. Introduction

Gold nanoparticles (AuNPs) are among the most exploited nanosized materials in biomedicine for cancer theranosis,[1–3] mostly due to the wide possibilities of chemical modification and tunable optical and thermal capacity.[1,4–7] The canonical collective resonance of electrons in the dielectric–metal interface upon the incidence of light of a wavelength larger than the nanoparticle diameter (localized surface plasmon resonance (LSPR), around 525 nm for spherical AuNPs) restricts their use in photo-thermal therapy (PTT) or photoacoustic imaging (PAI) as the wavelengths needed to efficiently engage plasmon resonance fall within the UV-visible spectrum, far from tissue transparency windows. LSPR nonetheless highly depends on nanoparticle size, shape and self-assembly. Gold nanoparticle interaction indeed affects their electronic and optical properties, thereby tuning the collective plasmonic response. When close enough (<2 nm), electron clouds from two nanoparticles collectively de-colocalize upon light incidence, and produce a red-shifted plasmon, *i.e.*, plasmonic coupling.[8–10] This process is indeed the basis for several chemical and biological sensor systems based on noble metal nanoparticles, specially AuNPs.[11,12] Although huge efforts have been made to control gold nanoparticle aggregation, and henceforth tune their physical properties, the process is still not well understood. Moreover, most of the approaches leading to NIR plasmon convey difficult and complex chemical steps that prevent the easy-scaling production of gold nanoparticles for clinical purposes.

To achieve plasmon coupling, various polymers, molecular ligands and electrolytes have been used to induce the aggregation of preformed AuNPs, and, therefore, the reduction of inter-particle space.[13–15] However, the lack of controllable aggregation affects the stability of the produced nanoparticle clusters over time. To cope with this issue, several methods have been applied based on the modification of the hydro-

Laboratoire Matière et Systèmes Complexes, UMR 7075, CNRS and Université Paris Diderot, 10 Rue Alice Domon et Léonie Duquet, 75205 Paris Cedex 13, France. E-mail: florence.gazeau@univ-paris-diderot.fr

†Electronic supplementary information (ESI) available. See DOI: 10.1039/c8nr09849b

This journal is © The Royal Society of Chemistry 2019

Published on 21 janar 2019. Downloaded by Fail Open on 7.5.2025 9:29:04 e paradites.

phobic/hydrophilic properties of chemical components[16] or the use of a polymer-directed synthesis of gold nanoparticles.[17] The latter is in fact a suitable method to achieve a controllable AuNP synthesis with respect to not only the size and coating, but also the extent of nanoparticle aggregation.

Polyethyleneimine (PEI) has been widely used for experimental gene transfection as it escapes the early endosomal compartment owing to the so-called 'sponge-effect'.[18] The high density of uncharged amines in PEI provokes protonation, hence a rapid and massive influx of Cl^- and water into the endosomes; the osmotic swelling of the endosome and swelling of the polymer due to the repulsion between the charges lead to an increase in internal pressure and membrane disruption. It thereby releases cargo into the cytoplasm, avoiding further degradation in the late endosomes upon fusion with lysosomes. PEI polycations also potentiate immune response by engaging and activating the mononuclear cell system (*i.e.* monocytes, macrophages) mediated by receptors such as Toll-like receptor 4. Consequently, a burst of pro-inflammatory cytokines and chemokines triggers further immune system activation, including T cells, dendritic cells, and B cells. Altogether, PEI has proven to be a potent adjuvant for the vaccination protocol either alone or in combination with Toll-like receptor activators.[19–22] Furthermore, PEI has been combined with a variety of inorganic nanoparticles to enhance or facilitate the therapeutic potential of the nanosystems by means of physical properties or biological activities.[23] Iron oxide nanoparticles have been coated with PEI and its derivatives to achieve multi-therapeutic potential that includes magnetic targeting, immune activation, and the intrinsic gene transfection ability of the polycation.[24–26] Likewise, PEI has been conjugated with preformed gold nanoparticles to ensure a nanocarrier for gene transfection.[27,28] However, these methods necessitate synthesis with at least three steps (*i.e.* AuNP synthesis, AuNP functionalization and AuNP clustering mediated by PEI) which is detrimental to the final yield and batch to batch reproducibility.[29–31] Therefore, a simplification of the synthesis procedures is highly desirable to obtain PEI-gold nanoparticle-based products that are easier to scale-up without impacting the plasmonic properties. In this direction, a few reports have described the intrinsic weak reductive potential of different PEIs to convert Au^{3+} into Au^{1+} and Au^0.[5,32–34] The influence of PEI concentration has also been addressed in terms of the Au crystal size, but no insightful mechanism has been described.[35] A detailed analysis of the PEI-dependent synthesis of AuNPs should shed some light on this matter. Other reports demonstrated that PEI can also influence AuNP size when used in a seed-mediated synthesis, highlighting the importance of elucidating how PEI concentration modulates the size of the final crystal product.[36] However, none of these studies evaluated the photothermal properties of the as-synthesized AuNPs for their use in the biomedical field. Importantly, there is a need to properly characterize how the PEI : Au ratio affects both nanoparticle size and aggregation. This study focuses on elucidating the effect of the PEI : Au ratio on gold nanoparticle growth and aggregation into fractal structures displaying collective plasmonic photothermal properties. We thoroughly analyzed the PEI-directed AuNP synthesis and obtained insightful results on the as-synthesized gold nanocomposite performance as a theranostic agent in a colorectal carcinoma (CRC) murine model. We demonstrated a differential kinetics for Au^{3+} reduction as well as different colloidal stability over time depending on the PEI concentration as monitored by small-angle X-ray scattering (SAXS), UV-visible spectroscopy and cryo-transmission electron microscopy (cryo-TEM). In addition, the PEI-assisted gold nanoparticles showed a quasi-fractal arrangement at PEI : Au ratios of 2.5 : 1 and 5 : 1, which led to the plasmonic coupling in the first NIR window. We further demonstrated that these fractal gold nanocomposites perform efficiently as thermal photoconverters both *in vitro* and *in vivo* in a CRC murine model, reinforcing their use in photo-ablative therapeutic approaches.

2. Materials and methods

2.1. Reagents and antibodies

Primary antibodies were anti-phospho-p44/p42 MAPK (9101S) from Cell Signaling and anti-vimentin (ThermoScientific, Pierce, MA3-745). YO-PRO-1 iodide (491/509, V23201), propidium iodide (PI, V23201), Hoechst 33342 (V23201), and DAPI (T3605) were all from Invitrogen. 25 kDa polyethyleneimine (PEI, 25 kDa, 40872-7) and $HAuCl_4$ salt (G402-5G) were purchased from Sigma-Aldrich.

2.2. AuPEI nanocomposite synthesis

The one-pot synthesis of polyethylenimine (PEI)-Au nanocomposites (AuPEI NCs) was carried out by mixing aqueous (1 mg mL^{-1}, Au^{3+}) $HAuCl_4$ solution with an aqueous solution of 25 kDa PEI at different [PEI] : [Au] ratios (0.5, 1, 2.5, 5 and 10) under constant magnetic stirring at room temperature (RT-synthesized). Reaction evolution was monitored by both visual color inspection and absorbance profiling in the UV-visible 350–800 nm wavelength range with a multimode plate reader (EnSpire, PerkinElmer). One year later, the resulting product was washed three times with distilled H_2O (ultracentrifugation, 10 000*g*) and dialysed against distilled H_2O using a 50 kDa cut-off membrane for the removal of excess polymer. Photothermal ablation assays *in vitro* and *in vivo* were carried out with 1-year-old nanoparticles.

2.3. Small-angle X-ray scattering (SAXS) characterization

Small angle X-ray scattering (SAXS) experiments were performed on the SWING beamline (SOLEIL synchrotron, Saint-Aubin, France) with a photon energy of 12 keV and a sample-to-detector distance of 6 m, leading to the following q-range: $0.0016 \leq q_{SWING}$ ($Å^{-1}$) ≤ 0.23 $Å^{-1}$. We recall that $q = (4\pi/\lambda)\sin\theta$, where 2θ is the scattering angle and λ = 1.033 Å is the wavelength. Samples were inserted into cylindrical quartz capillaries of 1.5 mm diameter that were sealed and left vertical in the field of gravity. The scattering patterns were always isotro-

Published on 21 janar 2019. Downloaded by Fail Open on 7.5.2025 9:29:04 e paradites.

pic and radially averaged to obtain the scattering curves $I(q)$. The scattering curves were fitted with SasView software (NSF DANSE), when stated with the sphere model to determine the radius of individual NPs or with the mass fractal model to determine the particle radius and the mass fractal dimension of the aggregated particles.

The sphere model gives the intensity scattered by a dilute dispersion of the spherical silica nanoparticle form factor, and is defined as follows:[37]

$$I(q) = \text{scale}\, V(\Delta\rho)^2 \left[3\frac{(\sin(qr) - qr\,\cos(qr))}{(qr)^3}\right]^2 + \text{background},$$

where scale is the volume fraction, V is the sample volume, r is the sphere radius, background is the background intensity and $\Delta\rho = (\rho_{Au} - \rho_{H_2O})$ is the difference in the scattering length density between the gold nanoparticles ($\rho_{Au} = 6.4608 \times 10^{-6}$ A^{-2}) and the solvent ($\rho_{H_2O} = 9.4691 \times 10^{-6}$ A^{-2}).

The mass fractal model is defined as follows:[38]

$$I(q) = \text{scale}\, P(q)S(q) + \text{background}$$

with

$$P(q) = F(qr)^2$$

$$F(qr) = \frac{3[\sin(qr) - qr\cos(qr)]}{(qr)^3}$$

$$S(q) = 1 + \frac{1}{(qr)^{D_m}} \frac{D_m \Gamma(D_m - 1)}{\left[1 + (q\zeta)^{-2}\right]^{\frac{D_m - 1}{2}}} \sin\left[(D_m - 1)\tan^{-1}(q\zeta)\right]$$

$$\text{scale} = \text{scale}_{\text{factor}} \left(\frac{4}{3}\pi r^3\right)(\rho_{Au} - \rho_{H_2O})^2$$

where r is the radius of the particles, Γ is the function defined as $\Gamma(x) = (x - 1)!$, ζ is the cut-off length and D_m is the mass fractal dimension.

2.4. Cryogenic transmission microscopy (Cryo-TEM)

AuPEI NCs were characterized by Cryo-TEM as published elsewhere.[39] Briefly, a 4 μL droplet of particle aqueous solution was deposited on a Quantifoil® (Quantifoil Micro Tools GmbH, Germany) holey carbon grid. The excess of liquid on the grid was absorbed with filter paper and the grid was quench-frozen quickly in liquid ethane to form a thin vitreous ice film. Once placed in a Gatan 626 cryo-holder cooled with liquid nitrogen, the samples were transferred to the microscope and observed at a low temperature (−180 °C). Cryo-TEM images were recorded with a 2k × 2k Gatan Ultrascan 1000 CCD camera (Gatan, USA), using a LaB_6 JEOL JEM2100 (JEOL, Japan) cryo-microscope operating at 200 kV (IMPMC, Sorbonne Université – CNRS UMR 7590, Paris, France). Images were taken with the JEOL low dose system (Minimum Dose System, MDS) to protect the thin ice film from any irradiation before imaging and to reduce the irradiation during the image capture.

2.5. Cell culture and cytotoxicity assay

The CT26 murine colon carcinoma cell line (ATCC, TIB-71) was cultured in complete DMEM supplemented with 10% fetal bovine serum (FBS), L-glutamine and penicillin/streptomycin. Subconfluent cells were incubated for 24 h with increasing concentrations of AuPEI NCs in complete DMEM. For the last 4 h, the Presto Blue cell viability reagent was added (1/10 final dilution; Presto Blue cell viability reagent, A13261; Invitrogen). Fluorescence was measured with a 535 nm excitation filter and a 615 nm emission filter. The fluorescence of complete DMEM incubated with Presto Blue was used as the background control. Cell viability was calculated according to the formula:

$$\text{Viability (\%)} = \frac{[\text{AuPEI treated cell fluorescence}] - [\text{medium fluorescence}]}{[\text{untreated cell fluorescence}] - [\text{medium fluorescence}]} \times 100\ \%$$

2.6. AuPEI NC photothermal conversion

For photo-thermal monitoring, 100 μL of the as-synthesized AuPEI NCs were extracted from the reaction tubes and subjected to laser irradiation (680 and 808 nm, 5 min, fluence 2 W cm^{-2}, height 4 cm from the liquid/air interface, Laser Diode Drivers, BWT). The temperature T was recorded with an infrared camera SC7000 from FLIR Systems. The optical specific absorption rate (SAR) was calculated as published before.[40,41] The initial temperature slope, *i.e.* the first 30 s dT/dt slope after laser switch-on, was measured, and the SAR was calculated according to: $\text{SAR} = \frac{Cv}{m}\frac{dT}{dt}$, where m is the total mass of Au in the sample, C is the specific heat capacity of the sample (C_{water} = 4185 J L^{-1} K^{-1}), and V is the sample volume.

2.7 Photothermal ablation in cell culture

Subconfluent CT26 cells were incubated with 5 μg mL^{-1} AuPEI NCs in complete medium for 24 h in 6-well cell culture plates and washed to remove the medium. The cells were then harvested, washed with PBS 1× and resuspended in 100 μL PBS 1× (500 μL tube). Absorbance was measured in a multimode plate reader (PerkinElmer, EnSpire), and immediately after, the cells dispersed in 100 μL PBS were subjected to an 808 nm beam laser for 5 min (fluence 2 W cm^{-2}, height 4 cm from the liquid/air interface, Laser Diode Drivers, BWT). Temperature was recorded with an infrared camera SC7000 from FLIR Systems.

To evaluate the photothermal ablation capability of AuPEI NCs on adherent cells, CT26 cells were seeded in 18-well slides (Ibidi) with a density of 2×10^4 overnight. After that, the AuPEI NC solution (5 μg mL^{-1}) was added in complete medium and incubated with cells for 24 h. After that, the medium was removed, and the cells were irradiated or not with an 808 nm laser at a power density of 2 W cm^{-2} for 15 min. The wells with only NIR irradiation and no treatment served as the negative groups. All CT26 cells were collected, washed with PBS, dyed with YO-PRO/PI/Hoechst Triple Stain (Invitrogen, V23201), and observed with confocal microscopy to evaluate cell necrosis and apoptosis.

 This journal is © The Royal Society of Chemistry 2019

Published on 21 janar 2019. Downloaded by Fail Open on 7.5.2025 9:29:04 e paradites.

2.8. *In vivo* colon carcinoma CT26 tumor model for photothermal therapy

Animal studies were conducted in agreement with the French guidelines for animal care in compliance with procedures approved by the Paris Diderot ethical committee for animal research. CT26 tumor-bearing BALB/c mice (6–8 weeks old), established by the subcutaneous injection of 1.5×10^6 CT26 cells (tumor size ≥5 mm), were randomized into six groups as follows: (i), untreated (n = 16); (ii), only 808 nm laser irradiation at ~2 W cm^{-2} for 15 min (height from tumor skin 4 cm, Laser Diode Drivers, BWT) (n = 10); (iii), AuPEI-2.5 NCs 20 μg per mouse injected intratumorally (40 μL, ~ 0.5 mg mL^{-1} Au) (n = 7); (iv) AuPEI-2.5 NCs 20 μg per mouse intratumorally plus laser irradiation (n = 6); (v), AuPEI-5 NCs 20 μg per mouse intratumorally (n = 14); (vi) AuPEI-5 NCs 20 μg per mouse intratumorally plus laser irradiation (n = 13). When necessary, the tumor was irradiated with a near infrared laser 24 and 48 h after AuPEI NC injection. All mice were anesthetized with isoflurane gas during the procedure according to the ethical animal treatment procedure. Additional groups were treated to compare the photothermal ablation efficiency of AuPEI-2.5 NCs to canonical spherical gold particles of 16 nm, $AuNP_{16\ nm}$. The mice were randomized into six groups (n = 4 to 7) as follows: (i), untreated (n = 7); (ii), only 808 nm laser irradiation at ~2 W cm^{-2} (n = 4); (iii), AuPEI-2.5 NCs 20 μg per mouse intratumorally (40 μL, ~ 0.5 mg mL^{-1} Au) (n = 7); (iv), AuPEI-2.5 NCs 20 μg per mouse intratumorally plus laser irradiation (n = 7); (v), $AuNP_{16\ nm}$ 20 μg per mouse intratumorally (30 μL) (n = 5); (vi) $AuNP_{16\ nm}$ 20 μg per mouse intratumorally (30 μL) plus laser irradiation (n = 5). The surface temperature was recorded with an infrared camera SC7000 from FLIR Systems during the treatment. CT26 tumor growth was monitored by measuring tumor dimensions with a caliper and the tumor volume v was calculated as follows: $v = \frac{LW^2}{2}$, as established elsewhere,[42] where L is the tumor length, and W is the tumor width. The ethical survival endpoint was considered as a tumor volume >1500 mm^3.

2.9. *In vivo* photoacoustic imaging (PAI)

To evaluate the PAI contrast efficiency of AuPEI NCs, 20 μg of AuPEI NC or 40 μg of $AuNP_{16\ nm}$ was injected into the CT26 tumor. All mice were anesthetized with gaseous anesthesia (isoflurane/air 4% induction and 1.5% during imaging) during the procedure according to the ethical animal treatment procedures. Mice were scanned with a PA system (VeVo®LZR SW2.2.0, VisualSonics, Inc., FUJIFILM, Institut Jacques Monod, Université Sorbonne Paris Cité, Paris, France) at different time intervals using a linear array transducer LZ550 (36 MHz center frequency, 32–55 MHz bandwidth, 44 μm axial resolution, 14 × 15 mm^2 image size) before and after injection to obtain PA images. The 3D B-mode and PA spectroscopic scans at 710 nm were performed on the subcutaneous tumors. Images were analyzed using VeVo®Lab and ImageJ software.

2.10. Histology and immunohistochemistry

Tumors were excised and fixed with 10% phosphate-buffered formalin at pH 7.4, dehydrated in graded ethanol solutions, and embedded in paraffin. Six-micrometer-thick sections were stained with hematoxylin and eosin for optical microscopy observation. For immunohistochemistry staining, the primary antibodies listed in Table 1 were used.

2.11. Statistical analysis

For all experiments, data were analyzed and depicted with GraphPad Prism software. Data are presented as mean ± SEM, and number of samples and independent experiments are stated in each figure caption for precision. When stated, data were analyzed with a two-tailed Mann–Whitney test under an assumption of the non-Gaussian distribution (nonparametric test), with 95% confidence, and $*p < 0.05$, $**p < 0.01$, $***p < 0.001$. Survival curves were compared using the Kaplan–Meier method and the p-value was calculated using the log rank test; $*p < 0.05$, $**p < 0.01$, and, $***p < 0.001$, 95% confidence, and the tumor volume was calculated using the two-way ANOVA test with Bonferroni's correction; $*p < 0.05$, $**p < 0.01$, and, $***p < 0.001$, 95% confidence.

3. Results and discussion

3.1. Kinetic analysis of AuPEI nanocomposite formation over 45 days

Polyethyleneimine (PEI) has been described as a reducing agent for gold nanoparticle synthesis,[32,34,43] but was more widely used in coating/modification steps on previously synthesized gold nanoparticles implicating a more potent reducing agent.[29,44,45] Here we thought to explore the optimal polymer concentration leading to gold nanocomposites exhibiting a fractal-like lattice, and, henceforth, a good aggregation-driven photo-thermal conversion efficiency without affecting nanoparticle stability. Since 25 kDa PEI is one of the most used polycations in several gene therapy approaches, we chose this polymer for determining its capacity as a dual Au-reducing and -capping agent, and the influence of polymer concentration on such features. As such, 1 mg mL^{-1} (~ 5 mM) of Au aqueous solution, made from $HAuCl_4 \cdot 3H_2O$, was mixed thoroughly with an equal volume of PEI at various concentrations (1, 2.5, and 5 mg mL^{-1}), and we followed the PEI-assisted Au^{3+} reduction for 45 days at room temperature. As shown in Fig. 1A (insets), the mixture changed immediately from light yellow to dark yellow in all cases, thus indicating the formation of Au-PEI complexes by the coordination of Au^{3+} cations by amine residues. As early as 1 h after mixing, gold

Table 1 Primary antibodies used for immunohistochemistry

Antibody	Clone	Dilution	Company
Phospho-Erk (p44/42)	Rabbit	1 : 500	Cell Signaling, 9101S
Ki67	Rabbit	1 : 1000	Abcam, ab15580

Published on 21 janar 2019. Downloaded by Fail Open on 7.5.2025 9:29:04 e paradites.

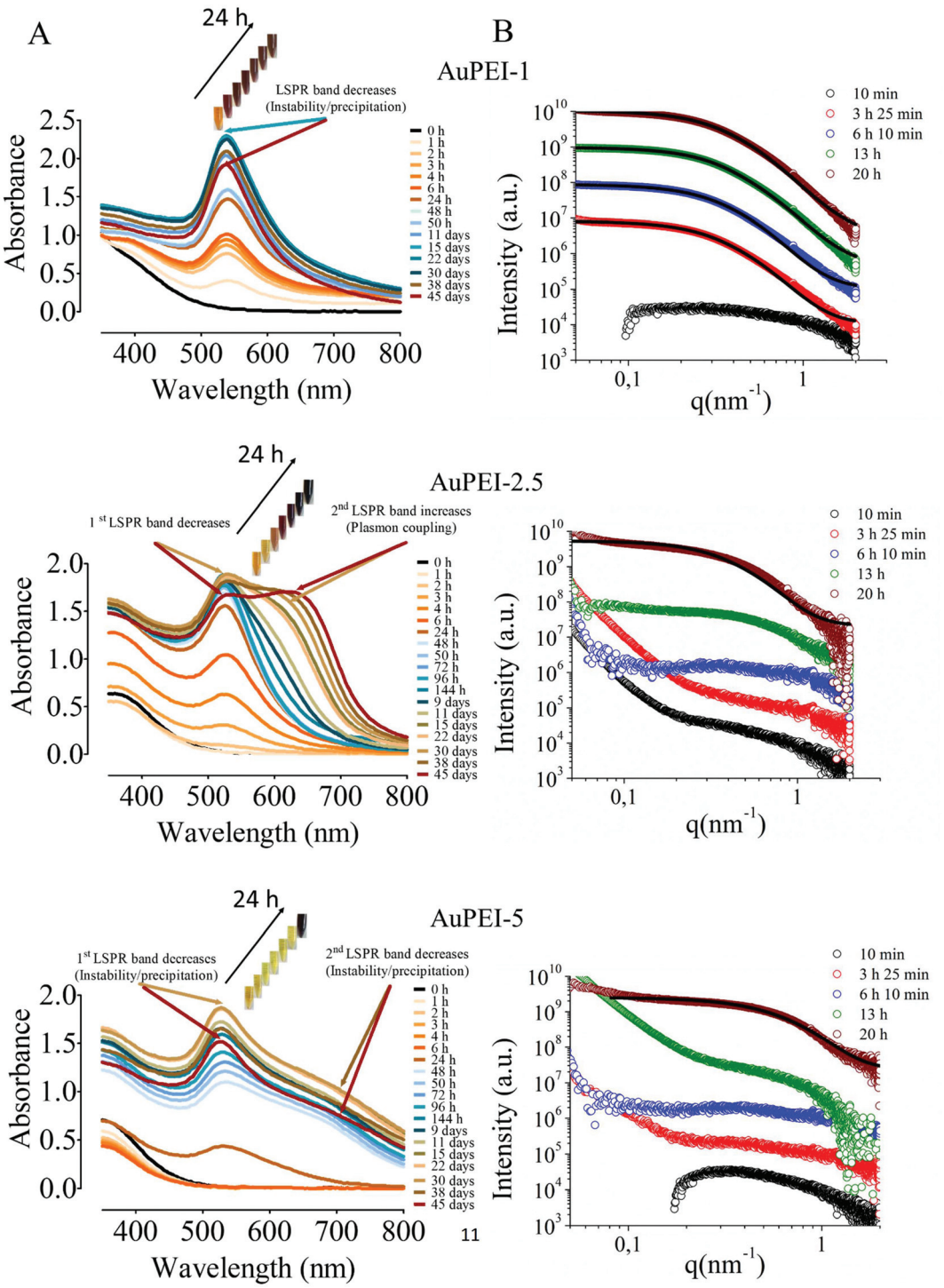

Fig. 1 AuPEI nanocomposite formation kinetics in the first 45 days as determined by (A) the UV-visible light absorbance profile (insets are the representatives of color inspection of reaction evolution within the first 24 h). (B) Time-resolved SAXS analysis in the first 20 h. The best fit by a spherical form factor model is depicted by black circles, corresponding to a mean diameter of 3.16 nm (PD 0.38) after 13 h and 5.18 nm (PD 0.40) at 20 h for AuPEI-2.5 and 3.72 nm diameter (PD 0.36) after 20 h for AuPEI-5. SAXS profiles have been displaced by a decade for better visualization.

nanoparticles were patent at a [PEI] : [Au^{3+}] ratio of 1, according to the appearance of a localized surface plasmon resonance (LSPR) band around 539 nm corresponding to the transversal mode of the as-synthesized particles, denoted as AuPEI-1 (Fig. 1A, top, and Fig. S1A†). Similar behavior was observed for the 2.5 : 1 ratio, in which case, the colloidal state of AuPEI-2.5 was evident after 3 h (Fig. 1A, middle). In contrast, AuPEI-5 did not show a concise transversal mode LSPR

 This journal is © The Royal Society of Chemistry 2019

Published on 21 janar 2019. Downloaded by Fail Open on 7.5.2025 9:29:04 e paradites.

band before 24 h (Fig. 1A, bottom, and Fig. S1A†). In order to widen the range of polymer concentrations, we investigated two more [PEI] : [Au^{3+}] ratios, 0.5 : 1 and 10 : 1 (Fig. S2†). It is worth noting that although AuPEI-0.5 exhibited an early production of nanoparticles attested by an LSPR peak at 569 nm, this peak decreased after 24 h (Fig. S2A and S2C†), suggesting that the scarce availability of a PEI capping agent leads to an unstable nanocomposite. In contrast, AuPEI-10 delayed the nanoparticle appearance until 48 h, and the formation of gold nanoparticle as measured by the evolution of the LSPR band at 539 nm was slower as compared to the other reaction mixtures (Fig. S2B and S2C†). This clearly shows that the polymer availability governs the kinetics of the nanoparticle onset. At longer time points, despite the increment of the AuPEI-1 primary LSPR band, it started decreasing after 15 days due to the formation of clear precipitates (Fig. 1A, top, and S1A†), leaving only a stable dispersion of larger objects after 30 days (Fig. S1A†). Such precipitation might be related to the limiting availability of the polymer as a capping agent as published elsewhere.[46] Altogether, the reduction of Au^{3+} and further nucleation into nanoparticles are influenced by the initial polymer concentration, whereby the lower the PEI concentration, the faster the initial reaction to the detriment of nanocomposite stability over time.

More interestingly, we identified an intermediate range of [PEI] : [Au^{3+}] ratios between 2.5 and 5 that gave rise to a second LSPR band falling in the NIR range and evolving concomitantly with the primary LSPR band (Fig. 1A). The LSPR bands of AuPEI-5 decreased a bit after 30 days most likely due to nanocomposite instability leading to a small precipitate formation. In contrast, AuPEI-2.5 gradually exhibited a NIR-falling shoulder after 9 days, that kept growing to the detriment of the primary LSPR band after 30 days, suggesting a stable clustering process rather than precipitation (Fig. 1A, middle). Importantly, we monitored absorbance at 680 nm wavelength to assess whether AuPEI can be used as a thermal nanoconverter in the NIR region. As shown in Fig. S1B,† AuPEI-5 absorbance 680 nm stepped up after 24 h of reaction reaching its maximum value after 30 days. In contrast, AuPEI-2.5 absorbance at 680 nm started increasing only after 10 days. Altogether, we revealed for the first time an experimental window that enables the synthesis of stable AuNP clusters with strong optical absorption above 680 nm by reducing Au^{+3} with PEI.

To confirm these results, we performed time-resolved small-angle X-ray scattering (SAXS) analysis (Fig. 1B). After 3 h of reaction, the SAXS profiles of AuPEI-1 depicted the formation of isolated spherical gold nanoparticles with a diameter of 5.6 nm and a polydispersity (PD) of 0.4. These characteristics did not change significantly after 6, 13 and 20 h of reaction (Fig. 1B, top). The appearance of nanoparticles was delayed when the polymer concentration was increased, and the SAXS intensity fit into a spherical core form factor with a diameter of 3.16 nm (PD 0.38) after 13 h and 5.18 nm (PD 0.40) at 20 h for AuPEI-2.5 and 3.72 nm diameter (PD 0.36) after 20 h for AuPEI-5, thereby confirming the absorbance profiling. Visual observation of the aggregates of AuPEI-2.5 and AuPEI-5 nanocomposites by CryoTEM at 30 days of reaction shows a size ~12.8 and ~10.8 nm, respectively (Fig. 2A). After 45 days, the SAXS profiles were consistent with a mass fractal model corresponding to the aggregates with mass fractal dimensions of 1.68 and 1.85, composed of particles with a diameter of 10.2 and 8.0 nm, respectively (Fig. 2B). This behavior is consistent with the appearance of the secondary LSPR band due to a plasmonic coupling between the adjacent nanoparticles (Fig. 1A).

We then investigated if the AuPEI nanocomposites obtained at 45 days can be efficient light to heat nanoconverters when excited with an 808 nm laser that is well adapted to penetrate living tissue. AuPEI-2.5 and −5 at a concentration of [Au] = 1 mg mL^{-1} showed an efficient conversion of NIR light (λ 808 nm, 2 W cm^{-2}) into heat, with an increase of ΔT >15 °C and >20 °C, respectively, outperforming AuPEI-1 (ΔT < 5 °C) (Fig. 2C), in line with the appearance of the second LSPR band in the NIR region due to the clustering-induced plasmon coupling.

A kinetic study of the absorption properties suggests that nanoparticle clustering keeps evolving after 30/45 days for AuPEI-2.5 and −5, forming NIR plasmonic nanoclusters. We thus investigated the colloidal structure and plasmonic properties of stable one-year-old AuPEI NCs. Interestingly, cryoTEM imaging shows the formation of quasi-fractal nanoclusters, consisting of densely packed nucleation centers from which nanoparticle-forming branches emerge (Fig. 3A). AuPEI-2.5 (TEM averaged core diameter, 11.3 nm, Fig. 3A, left) self-arranged into large globular clusters exhibiting an averaged diameter of 233 nm (Fig. 3B), while AuPEI-5 (TEM averaged core diameter, 9.6 nm, Fig. 3A, middle) exhibited a less prominent nanoparticle clustering (averaged cluster diameter, 77 nm, Fig. 3B). For comparison, we chose AuPEI-10 NCs which do not show a secondary LSPR band. AuPEI-10 (TEM averaged core diameter, 22 nm) tended to self-arrange in chains with exiguous ramifications (Fig. 3A, right), therefore less packed (TEM averaged cluster diameter, 64.7 nm, Fig. 3B). Accordingly, the number of nanoparticles per cluster decreased as we increased the [PEI] : [Au] ratio, showing an average number of 71, 35 and 7 nanoparticles per cluster, respectively (Fig. 3B). These structural characteristics translate into the appearance of the secondary LSPR band we observed during the nanocomposite formation (Fig. 3C). SAXS analysis confirmed the fractal arrangements adopted by AuPEI NCs owing to the SAXS intensity fitting the mass fractal model. According to this model, AuPEI-5 displayed the densest structure with a mass fractal dimension D_m of 1.9, in comparison with 1.6 and 1.0 for AuPEI-2.5 and AuPEI-10, respectively (Fig. 3D). As expected, 1-year-old AuPEI-2.5 and −5 nanocomposites showed a better photothermal conversion upon 808 nm laser irradiation (fluence 2 W cm^{-2}, 5 min, [Au] = 0.5 mg mL^{-1}) as compared to their counterpart AuPEI-10 (Fig. 3E), with a ΔT ~17, ~18, and ~11 °C, and a SAR_{808} = 1669.8, 1988.7, and 1166.7 W g^{-1} of gold, respectively. Altogether, this kinetic study shows that the quasi-fractal clusters of AuNPs can be obtained in water using branched PEI as

Published on 21 janar 2019. Downloaded by Fail Open on 7.5.2025 9:29:04 e paradites.

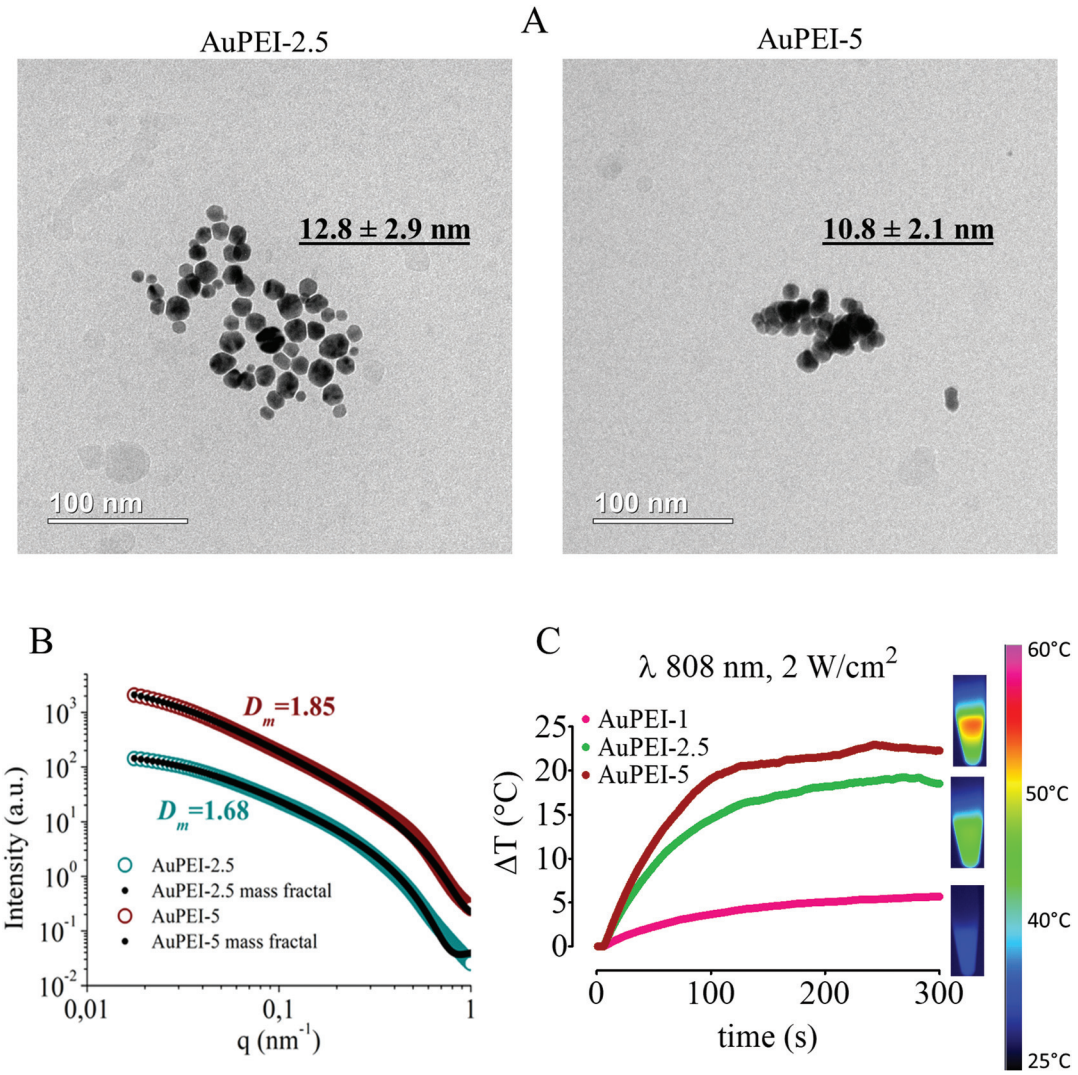

Fig. 2 AuPEI nanocomposite formation after 30 days as determined by (A) cryo-TEM imaging of the nanocomposites at 30 days. Numbers indicate the gold nanoparticle's mean core diameter. (B) SAXS analysis of the AuPEI nanocomposites after 45 days of reaction. The best fit using the mass fractal model is depicted by black circles (core diameter of 10.2 nm, ζ = 34,1 nm, and D_m = 1.68) and (core diameter of 8.0 nm, ζ = 47.8 nm, and D_m = 1.85), respectively, for AuPEI-2.5 and for AuPEI-5. (C) Temperature increase in a suspension of 45-day-old AuPEI at [Au] = 1 mg mL^{-1} upon laser irradiation (808 nm, 2 W cm^{-2}, 5 min).

the reducing agent in a well-defined range of concentrations. We hypothesize that at lower PEI concentrations, there is not enough amine residues to stabilize the Au crystals, thus limiting seeding and nucleation and triggering AuNP precipitation. In contrast, at higher PEI concentrations, the high density of amine residues leads to the spaced formation/nucleation of AuNPs and, therefore precludes plasmon coupling. However, an intermediate polymer concentration provides enough amine residues to reduce Au^{3+} and further nucleate and form clusters of AuNPs. Interestingly, the kinetics of nanoparticle formation (short times) and aggregation (long times) are different. After one year, the local structure and the global size of clusters are well defined depending on the [PEI] : [Au] ratio, allowing the optimization of the photothermal conversion efficiency.

3.2. Photo-thermal conversion efficiency *in vitro*

To appreciate the theranostic potential of the AuPEI nanocomposites, we first tested the viability of CT26 colon carcinoma cells exposed to AuPEI for 24 h, in the absence of any light exposure. AuPEI-2.5, 5 and 10 did not induce appreciable CT26 cell death in the concentration range assessed (3.9–250 μg mL^{-1}) (Fig. S3†). Since AuPEI-5 exhibited the most efficient thermal conversion as a colloidal suspension as compared to its counterparts, supported by the highest mass fractal dimension (1.9), we assessed the thermal conversion performance of AuPEI-5-loaded colorectal cancer cells CT26 *in vitro* either in a cell suspension or as adherent cells (Fig. 4A). To assess the photothermal conversion in cell pellet mimicking tumors, cell monolayers were incubated with

 This journal is © The Royal Society of Chemistry 2019

Published on 21 janar 2019. Downloaded by Fail Open on 7.5.2025 9:29:04 e paradites.

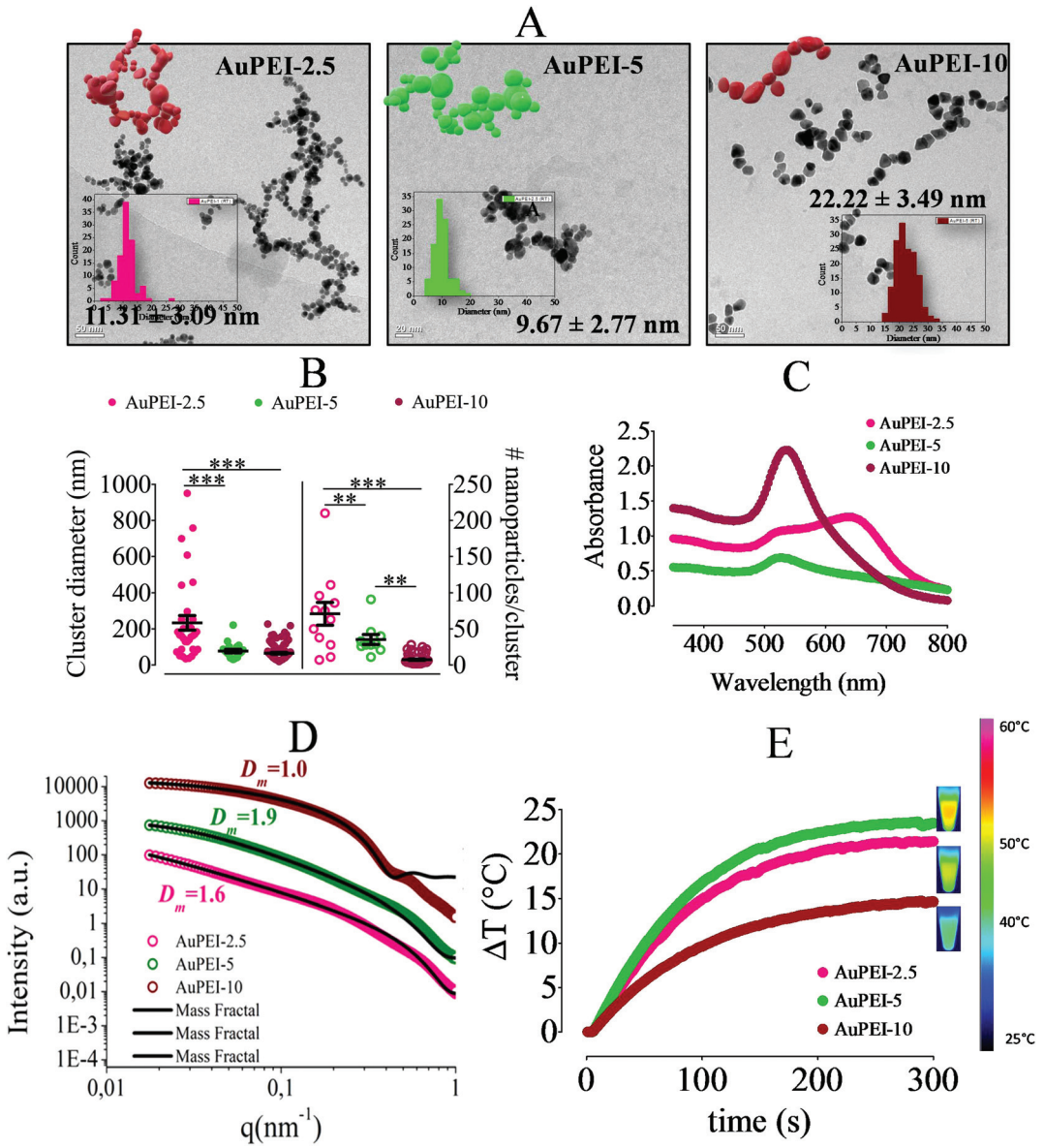

Fig. 3 Physical–chemical analysis of 1-year-old AuPEI nanocomposites. (A) Cryo-TEM imaging of AuPEI nanocomposites showing the quasi-fractal states of gold nanoparticle colloids. The inset summarizes the diameter measurement and depicts a 3-D model for nanoparticle aggregates. (B) AuPEI cluster size (left) and the number of nanoparticles per cluster (right), according to cryo-TEM images. A one-way ANOVA test was used, $^{**}p < 0.01$, and, $^{***}p < 0.001$, with Tukey's post-test, 95% confidence. (C) UV-visible absorbance profile. (D) Small angle X-ray scattering (SAXS) profile for AuPEI nanocomposites. The best mass fractal model fit is depicted by black circles (AuPEI-2.5: core diameter of 8.6 nm, ζ = 122.17 nm, and D_m = 1.6), (AuPEI-5: core diameter of 9.0 nm, ζ = 36.8 nm, and D_m = 1.9), and (AuPEI-10: core diameter of 20 nm, ζ = 33.9 nm, and D_m = 1.0). (E) Photothermal efficiency of AuPEI nanocomposites ([Au] = 0.5 mg mL^{-1}, laser 808 nm 2 W cm^{-2}, 5 min).

5 μg mL^{-1} (total Au, 5 μg) AuPEI-5 for 24 h, washed, harvested and resuspended (cells from one confluent well from a 6-well plate were resuspended in 100 μL PBS 1×). Interestingly, the suspension of AuPEI-5-loaded cells displayed a wide absorbance band with higher absorbance in the first NIR region as compared to the non-loaded cells (Fig. 4B). Consequently, a good thermal conversion was observed when the 100 μL suspension of AuPEI-loaded tumor cells was subjected to an 808 nm laser (5 min, fluence 2 W cm^{-2}), with a $\Delta T > 15$ °C as compared to $\Delta T < 2$ °C for the non-loaded cells (Fig. 4C). We also tested the cytotoxic effect of intracellular photothermal conversion on the monolayers of adherent CT26 cells incubated with the AuPEI-5 nanocomposites for 24 h and washed before 808 nm laser irradiation (15 min, 2 W cm^{-2}). Although no temperature increase could be observed in the cell culture medium, we observed an increase in apoptosis and, to a lesser extent, in the necrosis rate of irradiated AuPEI-5-loaded CT26 cells as compared to the non-irradiated counterparts (Fig. 4D and E).

Collectively, the AuPEI nanocomposites efficiently induced cell death in the murine colorectal cell line CT26, suggesting

Published on 21 janar 2019. Downloaded by Fail Open on 7.5.2025 9:29:04 e paradites.

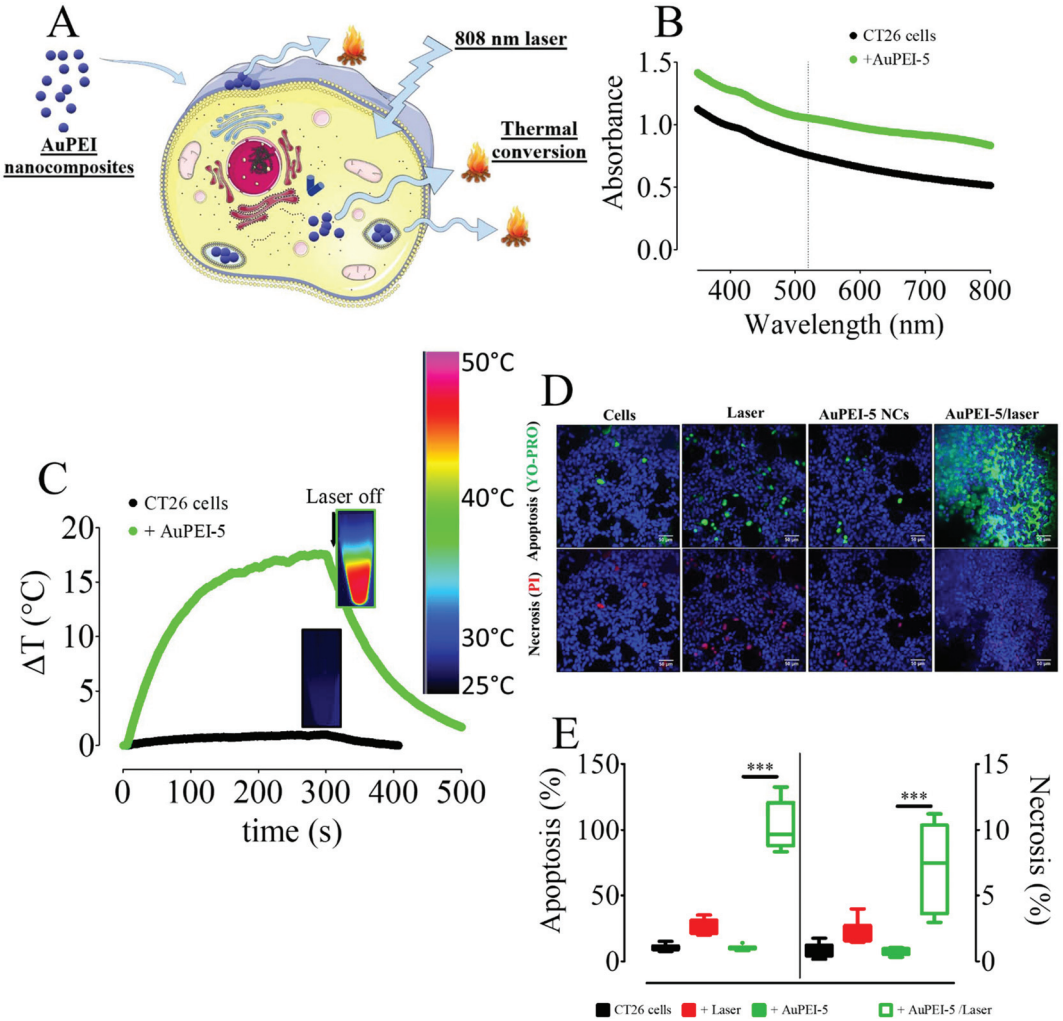

Fig. 4 Photo-thermal conversion. (A) General scheme depicting AuPEI-loaded CT26 cells' photo-thermal conversion. (B) Absorbance profile of AuPEI-5-loaded CT26 cells in comparison with non-loaded cells. (C) Representative temperature increase upon 808 nm laser irradiation of AuPEI-5 NCs associated with cells for 5 min and a fluence of 2 W cm^{-2}. (D) Representative CT26 pictograms for apoptosis and necrosis markers; and (E) cell viability of CT26 cells upon laser irradiation. *$p < 0.05$, **$p < 0.01$, and, ***$p < 0.001$, the two-way Mann–Whitney test, 95% confidence.

their usefulness for *in vivo* photothermal therapy in this model.

3.3. Photoacoustic imaging and anti-tumor photothermal ablation efficacy *in vivo*

Once the performance of the AuPEI-5 nanocomposite as a photo-converter and photothermal ablation at the cellular level was established, we determined their photothermal therapeutic effects and photoacoustic imaging in a mouse colorectal tumor model based on the CT26 cell line. As shown in Fig. 5A, CT26 cells were inoculated in the mouse's right flank and once the tumor reached ~250 mm^3 (10 days), the mice were intratumorally (i.t.) injected with the AuPEI nanocomposites (20 μg, Au). Immediately after i.t. injection, a clear photoacoustic signal (~710 nm) was observed intratumorally due to the AuPEI NCs that persisted after 24 h (Fig. 5B). The 710 nm PA signal coincided with the maximum PA signal peak according to the profile of the agarose phantoms of the AuPEI-5 nanocomposites (Fig. S4†). Then, the tumor was subjected to laser irradiation (808 nm-laser, 15 min, fluence 2 W cm^{-2}), and the tumor growth was monitored. In accordance, when irradiated, the temperature increased locally ($T > 50$ °C) for the AuPEI-5 injected tumors whereas the non-injected tumors showed temperatures less than 40 °C (Fig. 5C). As a result, tumor growth was delayed in the AuPEI-5 plus laser treatment group, with observable photothermal-ablation in most cases (Fig. 5D and E), in comparison with the control groups. We did not notice an apparent weight loss during the experiment (Fig. S5†). Collectively, the CT26-bearing mouse survival rate was significantly prolonged for the AuPEI-5 plus laser treatment cohort ($^{\#}p = 0.0199$, hazard ratio 5.875, 95% CI of the ratio, 1.323 to 26.09) as compared to either untreated mice or only the AuPEI-treated mice (**$p = 0.0088$, hazard ratio 7.354, 95% CI of the ratio, 1.61 to 33.41) (Fig. 5F). It is worth men-

 This journal is © The Royal Society of Chemistry 2019

Published on 21 janar 2019. Downloaded by Fail Open on 7.5.2025 9:29:04 e paradites.

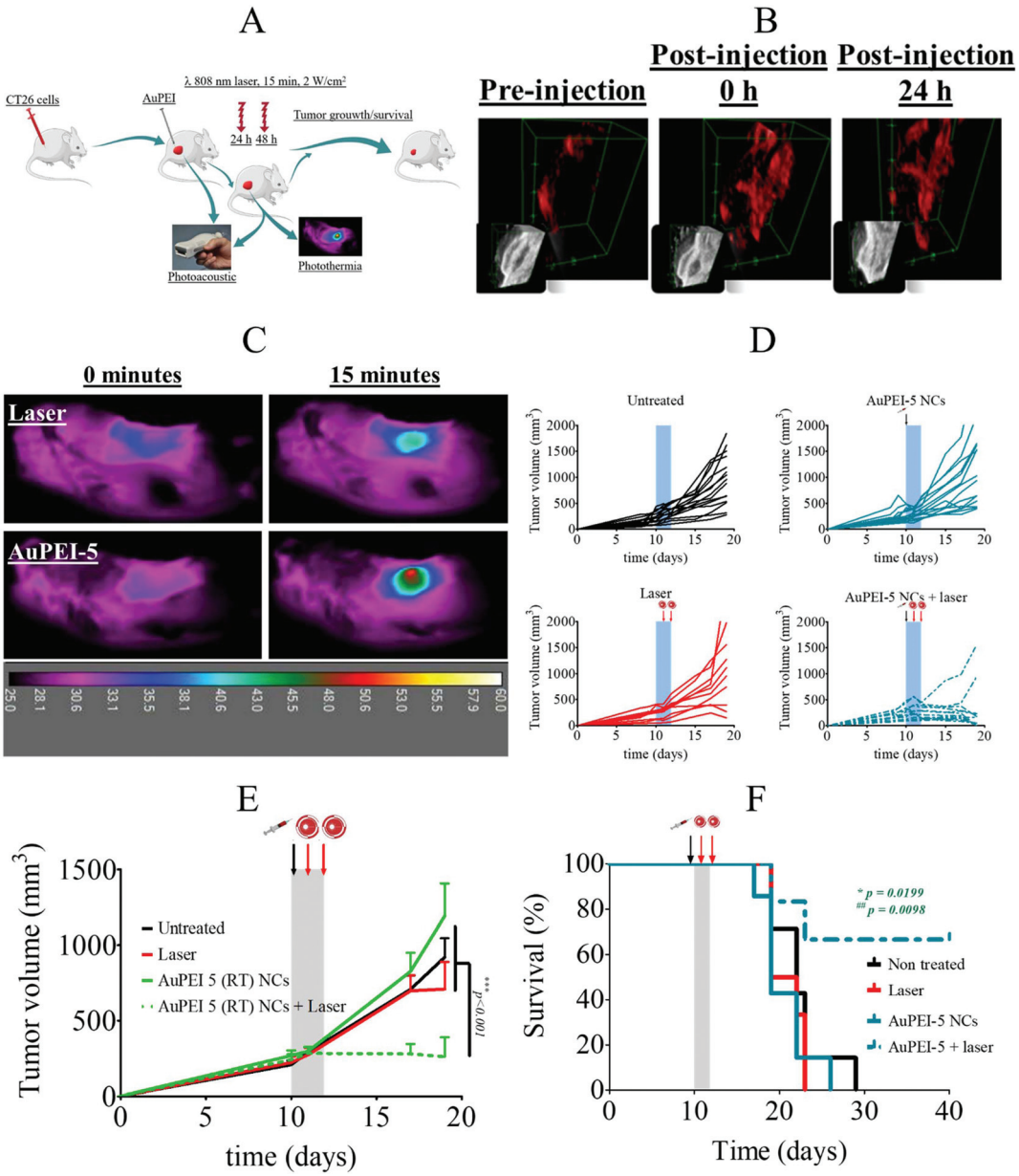

Fig. 5 *In vivo* anti-tumor efficiency and photoacoustic imaging of AuPEI nanocomposites. (A) *In vivo* experimental procedure on the subcutaneous CT26 tumor model. (B) Photoacoustic signal at 710 nm of the AuPEI-5 nanocomposites upon intratumoral injection in CT26 tumors. (C) Representative temperature profile of the tumor surface upon irradiation with an 808 nm laser at 2 W cm^{-2} for 15 minutes for a representative AuPEI-5-injected tumor and a non-injected tumor. (D) Individual tumor growth curves without (upper) and with (lower) laser irradiation. (E) Average tumor growth for different treatment groups (untreated, n = 16; laser, n = 10; AuPEI 5, n = 14; and, AuPEI 5/laser, n = 13). Tumor growth over time was compared using the two-way ANOVA test with Bonferroni's correction; *p < 0.05, **p < 0.01, and, ***p < 0.001, 95% confidence. (F) Survival curves per treatment (survival endpoint was reached when the tumor volume was 1500 mm^3), where differences were determined by the Kaplan–Meier method and the p value was calculated using the log-rank test; *p < 0.05, **p < 0.01, and, ***p < 0.001, 95% confidence.

tioning that AuPEI-2.5 NCs also showed good tumor ablative potential *in vivo* in agreement with their secondary LSPR band, inhibiting tumor growth and improving animal survival (Fig. S6†).

Tumor tissue analysis revealed an increase in necrotic areas upon laser irradiation (Fig. 6A and B) accompanied by an inhibition of tumor cell proliferation after AuPEI-5 /laser treatment as measured by proliferation marker Ki67 staining (Fig. 6A–C). In agreement, the phospho-p44/42 MAPK expression was decreased when tumors were subjected to the AuPEI-5 plus laser (Fig. 6A–D). p44/42 MAPK is involved in several signaling pathways, including tumor cell proliferation and survival, and acts as a link between external signals and intracellular molecular pathways.[47,48] Thus, the reduction of the activated p44/42 MAPK signaling pathway could contribute to the observed tumor growth inhibition.

Published on 21 janar 2019. Downloaded by Fail Open on 7.5.2025 9:29:04 e paradites.

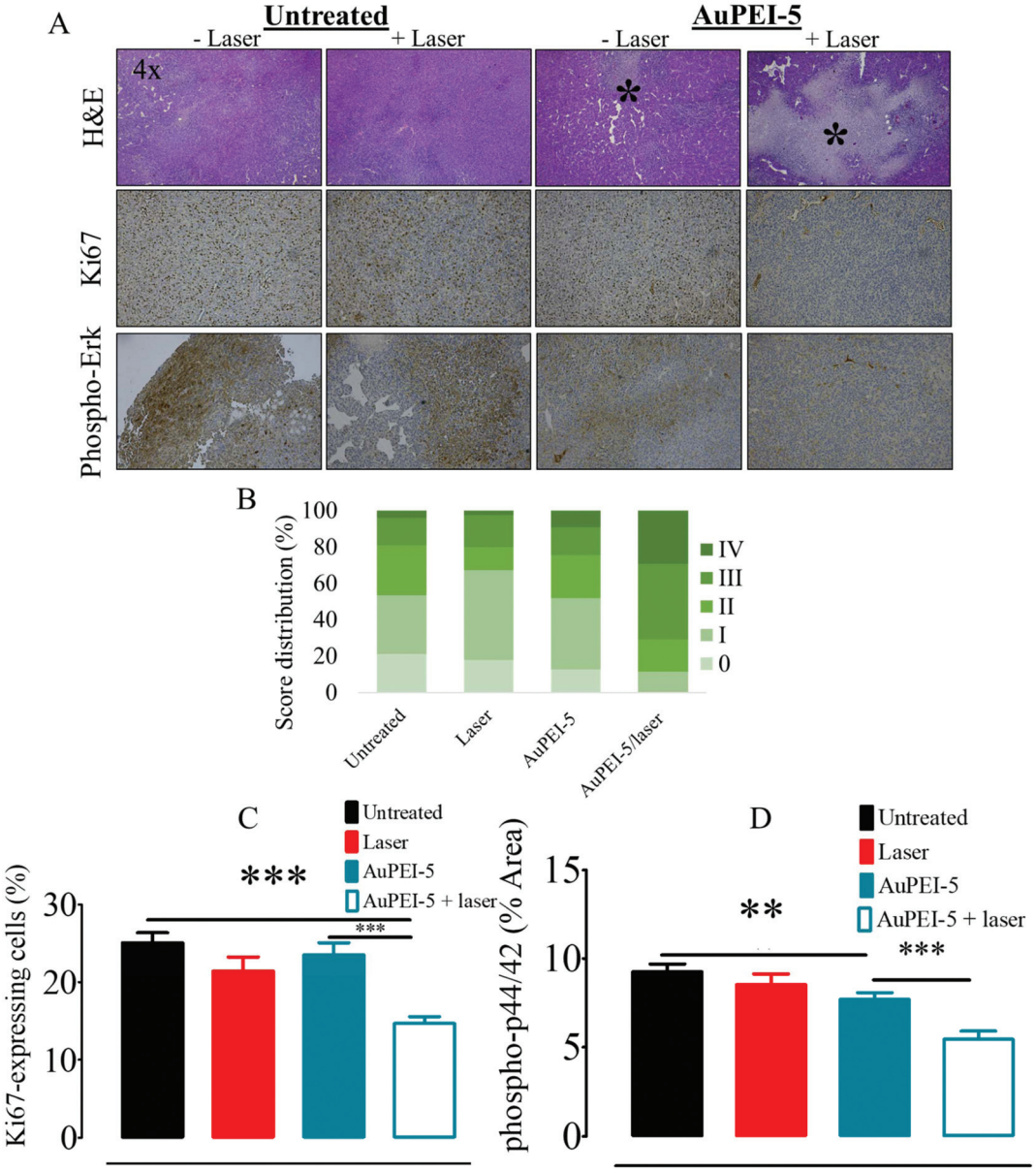

Fig. 6 Immuno-histochemical analysis of molecular signaling pathways in tumor tissues. (A), Representative H&S, Ki67 and phospho-p44/42 staining images according to each treatment. Summary of (B) the necrosis level, (C) Ki67-expressing percentage cells (n = 3 for a total image number of: Control, 52; laser, 38; AuPEI-5, 38; AuPEI-5/laser, 25), and (D) percentage of phospho-Erk expression (n = 3 for a total image number of: Control, 80; laser, 39; AuPEI-5, 54; AuPEI-5/laser, 19). More than 20 tumor sections were photographed for an appropriate semi-quantitative analysis of staining, *p < 0.05, **p < 0.01, and, ***p < 0.001, the two-way Mann–Whitney test, 95% confidence.

To rule out whether similar photothermal-ablation efficacy can be achieved by using canonical spherical AuNPs, we made an *in vivo* comparison between AuPEI-5 and spherical citrate-coated 16 nm diameter gold nanoparticles, $AuNP_{16\ nm}$, which exhibited a dispersed colloidal state (Fig. S7†). Following a similar *in vivo* procedure to that aforementioned, we observed that AuPEI-5 outperformed $AuNP_{16\ nm}$ in ablating the CT26 established tumors as measured by the tumor growth rate; the tumor volume for AuPEI-5 plus the laser cohort was 45.1 mm^3, while $AuNP_{16\ nm}$ plus the laser cohort exhibited a tumor volume of 1054.5 mm^3 at the same time (Fig. 7A and B). Likewise, the tumor weight for AuPEI-5 plus the laser cohort was ~6 μg compared to the $AuNP_{16\ nm}$ plus the laser cohort that exhibited an averaged tumor weight of 876 μg (Fig. 7C).

It has been stated that gold nanoparticle aggregation strongly affects their endocytosis, pivotal to the photo-thermal performance *in vivo*. Aggregated gold nanoparticles can indeed show a faster cellular endocytosis rate as compared to well-dispersed nanoparticles, leading to an earlier and more abundant intracellular nanoparticle clustering.[49] Furthermore, the size of agglomerates determines the intracellular movement of nanoparticles by reducing their speed,[50] which may lead to an

 This journal is © The Royal Society of Chemistry 2019

Published on 21 janar 2019. Downloaded by Fail Open on 7.5.2025 9:29:04 e paradites.

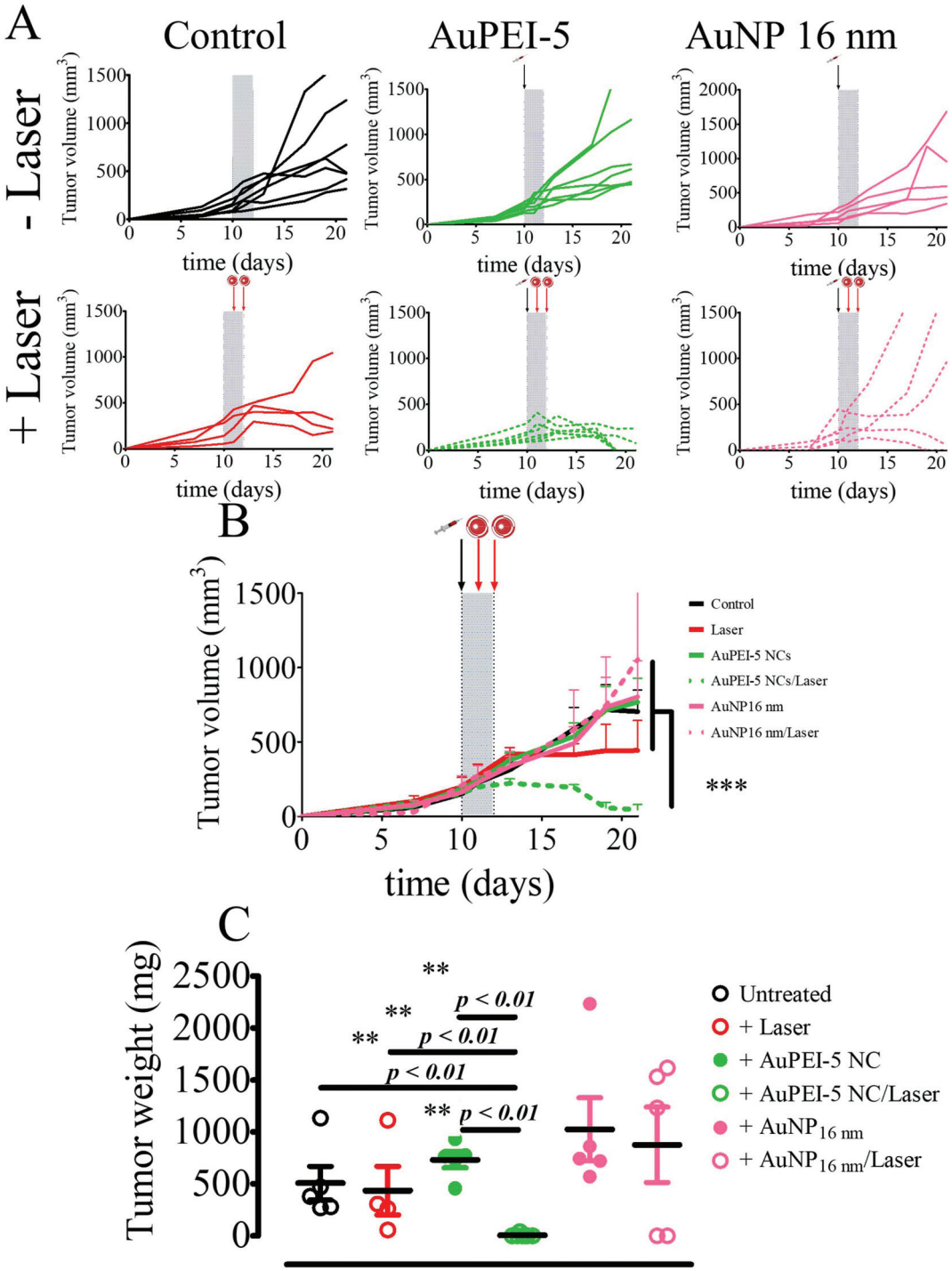

Fig. 7 *In vivo* photoablation performance comparison between AuPEI-5 (RT) and citrated AuNPs. (A) Individual tumor growth, and, (B) summary of tumor growth per treatment. (untreated, $n = 7$; laser, $n = 4$; AuNP 16 nm, $n = 5$; AuNP 16 nm/laser, $n = 5$; AuPEI 5 (RT), $n = 7$; and, AuPEI 5/laser, $n = 7$). Tumor growth over time was compared using the two-way ANOVA test with Bonferroni's correction; $^{*}p < 0.05$, $^{**}p < 0.01$, and, $^{***}p < 0.001$, 95% confidence. (C) Tumor weight at the endpoint (21 days). $^{*}p < 0.05$, $^{**}p < 0.01$, and, $^{***}p < 0.001$, the two-way Mann–Whitney test, 95% confidence.

increment in the intracellular retention time. We indeed observed that despite the detection of the $PA_{710\ nm}$ signal from $AuNP_{16\ nm}$ immediately after i.t. injection in the CT26 tumor *in vivo*, 24 h later nanoparticles appeared to have cleared from the inner tumor mass (Fig. S8†), in contrast to AuPEI-5 which the $PA_{710\ nm}$ signal persisted after 24 h (Fig. 6B). This persistent intratumoral presence of the AuPEI-5 nanocomposite might rely on the increase in the endocytosis rate, as mentioned before, and the endosomal escape of AuPEI-5 due to the PEI-triggered sponge-effect,[18,51,52] hence allowing the cyto-

Published on 21 janar 2019. Downloaded by Fail Open on 7.5.2025 9:29:04 e paradites.

plasmic accumulation of gold nanoparticles. However, a recently published report demonstrated the importance of intracellular aggregation to avoid exocytosis; the controllable induced intracellular aggregation through microRNA-21 of a binary gold nanoparticle system inhibited exocytosis leading to an improvement in the NIR-triggered thermal ablation.[53] Collectively, these facts prove the advantages that PEI-directed AuNP stable fractal aggregation imparts over dispersed AuNPs in terms of the photo-thermal performance *in vivo* due to both the plasmon coupling effect and the plausible increment of intracellular accumulation.

4. Conclusions

In this study, we characterized the formation of gold nanoparticles assisted by the polycation polyethyleneimine (PEI) in a time-resolved manner, as a facile and straightforward one-pot method to obtain plasmonic fractal nanocomposites. We were able to follow the Au^{3+} reduction and AuPEI nanocomposite formation by small-angle X-ray scattering profiling, UV-visible absorbance and photo-thermal conversion. As a result, we demonstrated that the initial polymer concentration impacts redox kinetics, where a 1 : 1 mass ratio favored the rapid formation of gold nanoparticle seeds and a higher polymer concentration not only slowed down the redox reaction, but also imparted the quasi-fractal aggregation of gold seeds. We indeed proved the fractal arrangements of the as-synthesized gold nanoparticles, where the $[PEI]:[Au^{3+}]$ = 5 mass ratio leads to the more compact aggregates, as determined by the mass fractal dimension, favoring plasmon coupling and NIR absorption. We demonstrated that the PEI-assisted self-assembly of the as-synthesized AuNPs leads to a plasmon coupling effect in an easy method without the need for further laborious modifications. Hence, AuPEI nanocomposites produced at a 5 : 1 mass ratio displayed good performance as NIR light nanoconverters for photoacoustic imaging and photo-ablation in a murine colon carcinoma model *in vitro* as well as *in vivo*. Furthermore, AuPEI-5 clearly outperformed a canonical spherical citrated gold nanoparticle in the thermal-ablation *in vivo*, suggesting the advantages of fractal gold nanostructures in cancer photo-reductive therapies. Collectively, this study sheds light on the kinetics of the one-pot PEI-assisted synthesis of fractal gold nanoparticles as theranostic agents in cancer.

The goal of our study was to develop plasmonic gold nanoparticles in an easy way (just by using the available reactants without further chemical modifications), with a high suitability for theranostic application. Typically, easily produced gold nanoparticles are sphere-shaped, but because of their monodisperse colloidal state, they are not convenient for NIR-based photo-ablative approaches. To induce a plasmonic coupling in the NIR region, spherical gold nanoparticles should coalesce, often leading to unstable colloids. Other gold nanoparticles with anisotropic shapes are suitable for NIR-based phototherapy, but their synthesis often requires more than one step and toxic additives. Therefore, the ideal scenario is to produce spherical gold nanoparticles in a simple way (one-pot) that also allows the as-produced nanoparticles to aggregate in a stable manner to ensure NIR-plasmon coupling without compromising stability. Thus, this one-pot synthesis outperforms others in terms of producing stable gold nanoparticle aggregates with an excellent NIR-based photo-ablative performance, and without introducing complex chemical surface modifications to induce such coalescence. It is worth noting that the work presented here adds significant applicability to PEI, apart from the extensively exploited features, *i.e.*, gene transfection and immunomodulating ability, increasing the possibility of combining phototherapy with other therapeutic approaches such as immunotherapy and gene therapy.

Conflicts of interest

The authors declare no competing financial interests.

Acknowledgements

VMA received a post-doc fellowship from the Association pour le Recherche contre le Cancer (ARC, Aides Individuelles, post-doctorant, dossier 20150603405). ANB received a PhD fellowship from the Institute thematique multi-organismes (ITMO) Cancer and the doctoral school Frontières du Vivant (FdV) – Programme Bettencourt. AB received a PhD fellowship from the doctoral school Physique en Ile de France (EDPIF). This work was supported by the ITMO-Inserm Plan Cancer 2014-2019. We are grateful to Christine Péchoux (INRA, UMR 1313, Plateforme MIMA2, Jouy en Josas, France) for the electron microscopy preparation and observations. The authors acknowledge synchrotron SOLEIL (SWING, SOLEIL, Saint-Aubin, France) for the SAXS beam time allocation and Thomas Bizien for his assistance.

References

1 W. Li and X. Chen, Gold Nanoparticles for Photoacoustic Imaging, *Nanomed.*, 2015, **10**(2), 299–320, DOI: 10.2217/nnm.14.169.

2 J. P. M. Almeida, A. Y. Lin, E. R. Figueroa, A. E. Foster and R. A. Drezek, In Vivo Gold Nanoparticle Delivery of Peptide Vaccine Induces Anti-Tumor Immune Response in Prophylactic and Therapeutic Tumor Models, *Small*, 2015, **11**(12), 1453–1459, DOI: 10.1002/smll.201402179.

3 L. A. Dykman, S. A. Staroverov, A. S. Fomin, V. A. Khanadeev, B. N. Khlebtsov and V. A. Bogatyrev, Gold Nanoparticles as an Adjuvant: Influence of Size, Shape, and Technique of Combination with CpG on Antibody Production, *Int. Immunopharmacol.*, 2018, **54**(June 2017), 163–168, DOI: 10.1016/j.intimp.2017.11.008.

4 R. Cheheltani, R. M. Ezzibdeh, P. Chhour, K. Pulaparthi, J. Kim, M. Jurcova, J. C. Hsu, C. Blundell, H. I. Litt,

 This journal is © The Royal Society of Chemistry 2019

Published on 21 janar 2019. Downloaded by Fail Open on 7.5.2025 9:29:04 e paradites.

V. A. Ferrari, *et al.*, Tunable, Biodegradable Gold Nanoparticles as Contrast Agents for Computed Tomography and Photoacoustic Imaging, *Biomaterials*, 2016, **102**, 87–97, DOI: 10.1016/j.biomaterials.2016.06.015.

5 F. Kretschmer, U. Mansfeld, S. Hoeppener, M. D. Hager and U. S. Schubert, Tunable Synthesis of Poly(Ethylene Imine)–Gold Nanoparticle Clusters, *Chem. Commun.*, 2014, **50**(1), 88–90, DOI: 10.1039/C3CC45090B.

6 M. H. Oh, J. H. Yu, I. Kim and Y. S. Nam, Genetically Programmed Clusters of Gold Nanoparticles for Cancer Cell-Targeted Photothermal Therapy, *ACS Appl. Mater. Interfaces*, 2015, **7**(40), 22578–22586, DOI: 10.1021/acsami.5b07029.

7 Y. Liu, J. He, K. Yang, C. Yi, Y. Liu, L. Nie, N. M. Khashab, X. Chen and Z. Nie, Folding Up of Gold Nanoparticle Strings into Plasmonic Vesicles for Enhanced Photoacoustic Imaging, *Angew. Chem., Int. Ed.*, 2015, **54**(52), 15809–15812, DOI: 10.1002/anie.201508616.

8 S. P. Scheeler, S. Mühlig, C. Rockstuhl, S. B. Hasan, S. Ullrich, F. Neubrech, S. Kudera and C. Pacholski, Plasmon Coupling in Self-Assembled Gold Nanoparticle-Based Honeycomb Islands, *J. Phys. Chem. C*, 2013, **117**(36), 18634–18641, DOI: 10.1021/jp405560t.

9 S. K. Ghosh and T. Pal, Interparticle Coupling Effect on the Surface Plasmon Resonance of Gold Nanoparticles: From Theory to Applications, *Chem. Rev.*, 2007, **107**(11), 4797–4862, DOI: 10.1021/cr0680282.

10 P. K. Jain and M. A. El-Sayed, Plasmonic Coupling in Noble Metal Nanostructures, *Chem. Phys. Lett.*, 2010, **487**(4–6), 153–164, DOI: 10.1016/j.cplett.2010.01.062.

11 V. Chegel, O. Rachkov, A. Lopatynskyi, S. Ishihara, I. Yanchuk, Y. Nemoto, J. P. Hill and K. Ariga, Gold Nanoparticles Aggregation: Drastic Effect of Cooperative Functionalities in a Single Molecular Conjugate, *J. Phys. Chem. C*, 2012, **116**(4), 2683–2690, DOI: 10.1021/jp209251y.

12 N. Uehara, Polymer-Functionalized Gold Nanoparticles as Versatile Sensing Materials, *Anal. Sci.*, 2010, **26**(12), 1219–1228, DOI: 10.2116/analsci.26.1219.

13 N. K. Kwon, T. K. Lee, S. K. Kwak and S. Y. Kim, Aggregation-Driven Controllable Plasmonic Transition of Silica-Coated Gold Nanoparticles with Temperature-Dependent Polymer-Nanoparticle Interactions for Potential Applications in Optoelectronic Devices, *ACS Appl. Mater. Interfaces*, 2017, **9**(45), 39688–39698, DOI: 10.1021/acsami.7b13123.

14 M. Sun, F. Liu, Y. Zhu, W. Wang, J. Hu, J. Liu, Z. Dai, K. Wang, Y. Wei, J. Bai, *et al.*, Salt-Induced Aggregation of Gold Nanoparticles for Photoacoustic Imaging and Photothermal Therapy of Cancer, *Nanoscale*, 2016, **8**(8), 4452–4457, DOI: 10.1039/C6NR00056H.

15 R. Poling-Skutvik, J. Lee, S. Narayanan, R. Krishnamoorti and J. C. Conrad, Tunable Assembly of Gold Nanorods in Polymer Solutions, *Appl. Nano Mater.*, 2017, 1–30.

16 I. Blakey, Z. Merican and K. J. Thurecht, A Method for Controlling the Aggregation of Gold Nanoparticles: Tuning of Optical and Spectroscopic Properties, *Langmuir*, 2013, **29**(26), 8266–8274, DOI: 10.1021/la401361u.

17 P. Alexandridis and M. Tsianou, Block Copolymer-Directed Metal Nanoparticle Morphogenesis and Organization, *Eur. Polym. J.*, 2011, **47**(4), 569–583, DOI: 10.1016/j.eurpolymj.2010.10.021.

18 Z. R. Amin, M. Rahimizadeh, H. Eshghi, A. Dehshahri and M. Ramezani, The Effect of Cationic Charge Density Change on Transfection Efficiency of Polyethylenimine, *Iran. J. Basic Med. Sci.*, 2013, **16**(2), 150–156.

19 T. Qin, Y. Yin, L. Huang, Q. Yu and Q. Yang, H9N2 Influenza Whole Inactivated Virus Combined with Polyethyleneimine Strongly Enhances Mucosal and Systemic Immunity after Intranasal Immunization in Mice, *Clin. Vaccine Immunol.*, 2015, **22**(4), 421–429, DOI: 10.1128/CVI.00778-14.

20 L. Song, D. Xiong, H. Song, L. Wu, M. Zhang, X. Kang, Z. Pan and X. Jiao, Mucosal and Systemic Immune Responses to Influenza H7n9 Antigen HA1-2 Co-Delivered Intranasally with Flagellin or Polyethyleneimine in Mice and Chickens, *Front. Immunol.*, 2017, **8**, 2–11, DOI: 10.3389/fimmu.2017.00326.

21 N. C. Sheppard, S. A. Brinckmann, K. H. Gartlan, M. Puthia, C. Svanborg, G. Krashias, S. C. Eisenbarth, R. A. Flavell, Q. J. Sattentau and F. Wegmann, Polyethyleneimine Is a Potent Systemic Adjuvant for Glycoprotein Antigens, *Int. Immunol.*, 2014, **26**(10), 531–538, DOI: 10.1093/intimm/dxu055.

22 C. Wu, J. Hopkins, M. Institutions, H. Yang, J. Hopkins, M. Institutions, C. M. Hospital, A. Monie, J. Hopkins, M. Institutions, *et al.*, *HHS Public Access*, 2015, **60**(8), 1085–1096, DOI: 10.1007/s00262-011-1013-7.

23 A. W. Li, M. C. Sobral, S. Badrinath, Y. Choi, A. Graveline, A. G. Stafford, J. C. Weaver, M. O. Dellacherie, T. Y. Shih, O. A. Ali, *et al.*, A Facile Approach to Enhance Antigen Response for Personalized Cancer Vaccination, *Nat. Mater.*, 2018, 1–7, DOI: 10.1038/s41563-018-0028-2.

24 M.-D. Hoang, H.-J. Lee, H.-J. Lee, S.-H. Jung, N.-R. Choi, M.-C. Vo, T.-N. Nguyen-Pham, H.-J. Kim, I.-K. Park and J.-J. Lee, Branched Polyethylenimine-Superparamagnetic Iron Oxide Nanoparticles(BPEI-SPIONs) Improve the Immunogenicity of Tumor Antigens and Enhance Th1 Polarization of Dendritic Cells, *J. Immunol. Res.*, 2015, **2015**, 1–9, DOI: 10.1155/2015/706379.

25 Y. Chen, G. Lian, C. Liao, W. Wang, L. Zeng, C. Qian, K. Huang and X. Shuai, Characterization of Polyethylene Glycol-Grafted Polyethylenimine and Superparamagnetic Iron Oxide Nanoparticles(PEG-g-PEI-SPION) as an MRI-Visible Vector for SiRNA Delivery in Gastric Cancer in Vitro and in Vivo, *J. Gastroenterol.*, 2013, **48**(7), 809–821, DOI: 10.1007/s00535-012-0713-x.

26 S.-L. Sun, Y.-L. Lo, H.-Y. Chen and L.-F. Wang, Hybrid Polyethylenimine and Polyacrylic Acid-Bound Iron Oxide as a Magnetoplex for Gene Delivery, *Langmuir*, 2012, **28**(7), 3542–3552, DOI: 10.1021/la204529u.

Published on 21 janar 2019. Downloaded by Fail Open on 7.5.2025 9:29:04 e paradites.

27 M. Thomas and A. M. Klibanov, Conjugation to Gold Nanoparticles Enhances Polyethylenimine's Transfer of Plasmid DNA into Mammalian Cells, *Proc. Natl. Acad. Sci. U. S. A.*, 2003, **100**(16), 9138–9143, DOI: 10.1073/pnas.1233634100.

28 B. Zhou, M. Shen, I. Bányai and X. Shi, Structural Characterization of PEGylated Polyethylenimine-Entrapped Gold Nanoparticles: An NMR Study, *Analyst*, 2016, **141**(18), 5390–5397, DOI: 10.1039/C6AN00841K.

29 J. Chen, H. Liang, L. Lin, Z. Guo, P. Sun, M. Chen, H. Tian, M. Deng and X. Chen, Gold-Nanorods-Based Gene Carriers with the Capability of Photoacoustic Imaging and Photothermal Therapy, *ACS Appl. Mater. Interfaces*, 2016, **8**(46), 31558–31566, DOI: 10.1021/acsami.6b10166.

30 J. Li, Y. Hu, J. Yang, P. Wei, W. Sun, M. Shen, G. Zhang and X. Shi, Hyaluronic Acid-Modified Fe3O4@Au Core/Shell Nanostars for Multimodal Imaging and Photothermal Therapy of Tumors, *Biomaterials*, 2015, **38**, 10–21, DOI: 10.1016/j.biomaterials.2014.10.065.

31 H. Huang, S. Barua, D. B. Kay and K. Rege, Simultaneous Enhancement of Photothermal Stability and Gene Delivery, *ACS Nano*, 2010, **4**(3), 1769–1770.

32 C. C. Chen and P. L. Kuo, Gold Nanoparticles Prepared Using Polyethylenimine Adsorbed onto Montmorillonite, *J. Colloid Interface Sci.*, 2006, **293**(1), 101–107, DOI: 10.1016/j.jcis.2005.06.051.

33 F. S. Mohammed, S. R. Cole and C. L. Kitchens, Synthesis and Enhanced Colloidal Stability of Cationic Gold Nanoparticles Using Polyethyleneimine and Carbon Dioxide, *ACS Sustainable Chem. Eng.*, 2013, **1**(7), 826–832, DOI: 10.1021/sc400028t.

34 S. Wen, F. Zheng, M. Shen and X. Shi, Synthesis of Polyethyleneimine-Stabilized Gold Nanoparticles for Colorimetric Sensing of Heparin, *Colloids Surf., A*, 2013, **419**, 80–86, DOI: 10.1016/j.colsurfa.2012.11.052.

35 T. Mikami, Y. Takayasu, J. Watanabe and I. Hirasawa, Influence of Polyethyleneimine Addition on Crystal Size Distribution of Au Nanocrystals, *Chem. Eng. Technol.*, 2011, **34**(4), 583–586, DOI: 10.1002/ceat.201000495.

36 A. Philip, B. Ankudze and T. T. Pakkanen, Polyethylenimine-Assisted Seed-Mediated Synthesis of Gold Nanoparticles for Surface-Enhanced Raman Scattering Studies, *Appl. Surf. Sci.*, 2018, **444**, 243–252, DOI: 10.1016/j.apsusc.2018.03.042.

37 A. Guinier and G. Fournet, *Small-Angle Scattering of X-Rays*, John Wiley Sons, N. Y., 1955.

38 P. W. Schmidt, Small-Angle Scattering Studies of Disordered, Porous and Fraetal Systems, Fractals Interdiscip, *J. Complex Geom. Nat.*, 1991, 414–435, DOI: 10.1107/S0021889891003400.

39 B. Fleury, M. A. Neouze, J. M. Guigner, N. Menguy, O. Spalla, T. Gacoin and D. Carriere, Amorphous to Crystal Conversion as a Mechanism Governing the Structure of Luminescent YVO4:Eu NANOPARTICLES, *ACS Nano*, 2014, **8**(3), 2602–2608, DOI: 10.1021/nn4062534.

40 A. Espinosa, R. Di Corato, J. Kolosnjaj-Tabi, P. Flaud, T. Pellegrino and C. Wilhelm, Duality of Iron Oxide Nanoparticles in Cancer Therapy: Amplification of Heating Efficiency by Magnetic Hyperthermia and Photothermal Bimodal Treatment, *ACS Nano*, 2016, **10**(2), 2436–2446, DOI: 10.1021/acsnano.5b07249.

41 R. Di Corato, A. Espinosa, L. Lartigue, M. Tharaud, S. Chat, T. Pellegrino, C. Ménager, F. Gazeau and C. Wilhelm, Magnetic Hyperthermia Efficiency in the Cellular Environment for Different Nanoparticle Designs, *Biomaterials*, 2014, **35**, 6400–6411, DOI: 10.1016/j.biomaterials.2014.04.036.

42 M. M. Tomayko and C. P. Reynolds, Determination of Subcutaneous Tumor Size in Athymic (Nude) Mice, *Cancer Chemother. Pharmacol.*, 1989, **24**(3), 148–154, DOI: 10.1007/BF00300234.

43 X. Sun, S. Dong and E. Wang, One-Step Preparation of Highly Concentrated Well-Stable Gold Colloids by Direct Mix of Polyelectrolyte and HAuCl4aqueous Solutions at Room Temperature, *J. Colloid Interface Sci.*, 2005, **288**(1), 301–303, DOI: 10.1016/j.jcis.2005.02.079.

44 W. Song, J. Du, T. Sun, P. Zhang and J. Wang, Gold Nanoparticles Capped with Polyethyleneimine for Enhanced SiRNA Delivery, *Small*, 2010, 239–246, DOI: 10.1002/smll.200901513.

45 Y. Lee, S. Hyeon, J. Seon, A. Maruyama, X. Chen and T. Gwan, Controlled Synthesis of PEI-Coated Gold Nanoparticles Using Reductive Catechol Chemistry for SiRNA Delivery, *J. Controlled Release*, 2011, **155**(1), 3–10, DOI: 10.1016/j.jconrel.2010.09.009.

46 C. H. Gammons, Y. Yu and A. E. Williams-Jones, The Disproportionation of Gold(I) Chloride Complexes at 25 to 200 °C, *Geochim. Cosmochim. Acta*, 1997, **61**(10), 1971–1983, DOI: 10.1016/S0016-7037(97)00060-4.

47 E. K. Kim and E. J. Choi, Pathological Roles of MAPK Signaling Pathways in Human Diseases, *Biochim. Biophys. Acta, Mol. Basis Dis.*, 2010, **1802**(4), 396–405, DOI: 10.1016/j.bbadis.2009.12.009.

48 K. Sasaki, T. Hitora, O. Nakamura, R. Kono and T. Yamamoto, The Role of MAPK Pathway in Bone and Soft Tissue Tumors, *Anticancer Res.*, 2011, **31**(2), 549–553.

49 E. Durantie, D. Vanhecke, L. Rodriguez-Lorenzo, F. Delhaes, S. Balog, D. Septiadi, J. Bourquin, A. Petri-Fink and B. Rothen-Rutishauser, Biodistribution of Single and Aggregated Gold Nanoparticles Exposed to the Human Lung Epithelial Tissue Barrier at the Air-Liquid Interface, *Part. Fibre Toxicol.*, 2017, **14**(1), 1–14, DOI: 10.1186/s12989-017-0231-3.

50 M. Liu, Q. Li, L. Liang, J. Li, K. Wang, J. Li, M. Lv, N. Chen, H. Song, J. Lee, *et al.*, Real-Time Visualization of Clustering and Intracellular Transport of Gold Nanoparticles by Correlative Imaging, *Nat. Commun.*, 2017, **8**(May), 1–10, DOI: 10.1038/ncomms15646.

 This journal is © The Royal Society of Chemistry 2019

51 N. D. Sonawane, F. C. Szoka and A. S. Verkman, Chloride Accumulation and Swelling in Endosomes Enhances DNA Transfer by Polyamine-DNA Polyplexes, *J. Biol. Chem.*, 2003, **278**(45), 44826–44831, DOI: 10.1074/jbc.M308643200.

52 Y. Yue, F. Jin, R. Deng, J. Cai, Y. Chen, M. C. M. Lin, H. F. Kung and C. Wu, Revisit Complexation between DNA and Polyethylenimine - Effect of Uncomplexed Chains Free in the Solution Mixture on Gene Transfection, *J. Controlled Release*, 2011, **155**(1), 67–76, DOI: 10.1016/j.jconrel.2010.10.028.

53 R.-C. Qian, J. Lv and Y.-T. Long, Controllable Aggregation-Induced Exocytosis Inhibition (CAIEI) of Plasmonic Nanoparticles in Cancer Cells Regulated by MicroRNA, *Mol. Pharm.*, 2018, **15**(9), 4031–4037, DOI: 10.1021/acs.molpharmaceut.8b00465.

Published on 21 janar 2019. Downloaded by Fail Open on 7.5.2025 9:29:04 e paradites.